

FERMI NATIONAL ACCELERATOR LABORATORY

SIST PROGRAM: FINAL PAPER

---

# A Simulation study of a totally active dual readout calorimeter

---

*Author:*  
Earle WILSON

*Supervisor:*  
Hans WENZEL

August 5, 2010

## CONTENTS

|   |           |
|---|-----------|
| <b>List of Tables</b> .....   | <b>0</b>  |
| <b>List of Figures</b> .....  | <b>0</b>  |
| <b>Introduction</b> .....   | <b>2</b>  |
| <b>The concept of the dual readout calorimeter</b> .....                    | <b>3</b>  |
| <b>Simulating the Dual Readout Calorimeter</b> .....                        | <b>4</b>  |
| Detector Configuration  | 4         |
| Physics Lists   | 4         |
| <b>Analysis</b> .....   | <b>5</b>  |
| Dual Readout Correction Process   | 5         |
| Taking a closer look at the digitization                                    | 6         |
| Analysis of minimum ionizing particle: Muon runs                            | 8         |
| Cell analysis   | 11        |
| The effect of energy threshold cuts on the energy resolution 20 GeV $\pi^-$ | 11        |
| <b>Conclusion</b> .....   | <b>12</b> |
| Summary of results and analysis   | 12        |
| Future work   | 12        |
| <b>References</b> .....   | <b>12</b> |

## LIST OF TABLES

|    |   |   |
|----|---|---|
| I  | Table showing detector configuration. ....                      | 4 |
| II | Table showing material properties of calorimeter crystals. .... | 4 |

## LIST OF FIGURES

|   |  |   |
|---|--|---|
| 1 | Figure showing an example of an EM shower in particle detector. The observed track is that of a 1 GeV electron .....   | 2 |
| 2 | Figure showing an example of an hadronic shower. The observed track is that of a 1 GeV $\pi^-$ .....   | 3 |
| 3 | Diagram representing a cross-sectional view of the proposed CCAL02 detector. The inner most rings represent the tracker. The subsequent layers are the EM calorimeter and its larger counterpart the HCAL calorimeter. Outside the HCAL calorimeter are magnetic coils and the muon chamber. The track seen in this diagram is that of a 5 GeV muon. ....                          | 3 |
| 4 | Figure showing the scintillation and cerenkov response for 1 GeV electron done for 10000 events. The figure on the left shows the Cerenkov response and the figure on the right shows the Scintillation response. The mean scintillation response is very close to the incident energy as one would expect. One should note the differences in the x-scales of the two plots. .... | 5 |
| 5 | Figure showing the plot of the scaled scintillation response $S$ against the scaled cerenkov response $C$ for a 1 GeV electron. ....   | 5 |
| 6 | Figure showing the plots of fraction $S/E$ against ratio $C/S$ for various energies. The top left plot is that for a 1 GeV electron. Going from left to right the plots shown are for 1, 2, 5, 10, 20, 50 and 100 GeV $\pi^-$ . The bottom right plot is that for all the energies combined. ....  | 6 |
| 7 | Figure displaying the fraction mean against each ratio for 1, 2, 5, 10, 20, 50 and 100 GeV $\pi^-$ . The relationships are parameterized by 4 <sup>th</sup> order polynomials whose equations are taken as the correction functions. The dashed line is the correction function obtain from the combination of all $\pi^-$ energies. ...   | 6 |
| 8 | Figure illustrating the plots of the corrected (pink line) and uncorrected (green line) scintillation energy response of 1, 2, 5, 10, 20, 50 and 100 GeV $\pi^-$ . ....  | 7 |

|    |   |    |
|----|---|----|
| 9  | Figure illustrating the raw(pink) and digitized (green) scintillation response for 1, 2, 5, 10, 20, 50 and 100 GeV $\pi^-$ . . . . .  | 7  |
| 10 | Figure showing the raw(pink) and digitized (black) correction function for combined $\pi^-$ energies. The relationships were parameterized by 4 <sup>th</sup> order polynomials. . . . .  | 7  |
| 11 | The above figure shows the raw(pink) and digitized (black) correction function for combined $\pi^-$ energies. The relationships were parameterized by 1 <sup>st</sup> order polynomials . . . . .   | 7  |
| 12 | Figure showing the raw(pink) and digitized (pink) corrected scintillation response for 1, 2, 5, 10, 20, 50 and 100 GeV $\pi^-$ . The correction function used was a 4 <sup>th</sup> order polynomial. . . . .   | 8  |
| 13 | Figure showing the raw(pink) and digitized (pink) corrected scintillation response for 1, 2, 5, 10, 20, 50 and 100 GeV $\pi^-$ . The correction function used was a 1 <sup>st</sup> order polynomial. . . . .   | 8  |
| 14 | Figure showing a simulated event of a 5 GeV muon going through the detector. The track begins at the inner radius of the the EM barrel, passes the through the Hadron barrel, then through the magnetic coils and finally through the muon chamber. . . . . | 9  |
| 15 | Figure showing pulse height seen per cell with and without the digitization cuts. . . . .   | 9  |
| 16 | Figure showing the pulse height as a function of time without the threshold cuts. . . . .   | 9  |
| 17 | Figure showing the pulse height as a function of time with the digitization threshold . . . . .   | 9  |
| 18 | Figure showing pulse height seen per cell for different energy threshold cuts in the ECAL. Here the energy thresholds were varied from $\frac{1}{50}$ , $\frac{1}{25}$ , $\frac{1}{10}$ , $\frac{1}{2}$ of a mip to 1 mip . . . . .                         | 9  |
| 19 | Figure showing shows pulse height seen per cell for different energy threshold cuts in the HCAL. Here the energy thresholds were varied from $\frac{1}{50}$ , $\frac{1}{25}$ , $\frac{1}{10}$ , $\frac{1}{2}$ of a mip to 1 mip . . . . .                   | 10 |
| 20 | Figure showing the fraction of energy lost per threshold cut. Here the energy thresholds were varied from $\frac{1}{50}$ , $\frac{1}{25}$ , $\frac{1}{10}$ , $\frac{1}{2}$ of a mip to 1 mip . . . . .  | 10 |
| 21 | Figure showing plots of the energy distribution per layer for the $\frac{1}{50}$ of a mip threshold cut. The first 8 layers are from the ECAL and the remaining 17 are from the HCAL (the 25 <sup>th</sup> layer is not shown). . . .                       | 11 |
| 22 | Figure showing plots of the corrected energy response for each threshold cut. . . . .   | 11 |
| 23 | Figure showing the sigma of the corrected energy response for each threshold cut. . . . .   | 11 |

# A Simulation study of a totally active dual readout calorimeter

Earle Wilson\*  
Columbia University  
(Dated: August 5, 2010)

In this research project, we seek to investigate the simulation and analysis process of a totally active dual readout calorimeter. The analysis of electron  $e^-$ , pi meson  $\pi^-$  and muon  $\mu$  simulations are presented. The dual readout correction process is explained in detail and the results from applying this process to 1, 2, 5, 10, 20, 50 and 100 GeV  $\pi^-$  are shown. The effect of energy threshold cuts on cell energy distributions are shown for the case of minimum ionizing particle (5 GeV muon) and later for a 20 GeV  $\pi^-$ . We show that the fine segmentation of this calorimeter puts constraints on the energy threshold cuts. The energy resolution of the corrected 20 GeV  $\pi^-$  response varied from  $\frac{E(\sigma)}{E} = \frac{0.11}{\sqrt{E}}$  for no threshold cuts to  $\frac{E(\sigma)}{E} = \frac{0.5}{\sqrt{E}}$  for a 1 m.i.p. threshold cut.

## INTRODUCTION

Calorimeters are instruments used to measure energy. In high energy physics these devices primarily function to measure the energy deposited by particles scattered from a high energy particle collision. Calorimeters can also assist in providing the trajectory and sometimes even the identity of incident particles.

When a very energetic particle traverses a dense medium it can often times generate a shower. There are two basic types of showers: *electromagnetic showers* and *hadronic showers*. Examples of these are shown in figure 1 and figure 2. Electromagnetic showers occur when high energy electrons, positrons or photons enter a medium at high energies and interact via pair production and the Bremsstrahlung process [1]. Pair production happens when high energy photons (above 5MeV) interact with an electron or an atomic nucleus and produce an electron-positron pair [2]. Bremsstrahlung radiation occurs when the electrons and positrons are deflected by electric field of the atoms as they move through the medium [2]. These photons then go on to produce more electron-positron pairs and the process is repeated.

The average energy loss by Bremsstrahlung in traversing a layer of thickness  $dx$  is given by

$$-\left(\frac{dE}{dx}\right)_{Brem} = 4\alpha N_0 \frac{Z^2}{A} r_e^2 E \ln\left(\frac{183}{Z^{1/3}}\right) = \frac{E}{X_0} \quad (1)$$

where  $N_0$  is Avogadro's number;  $Z$  and  $A$  are the atomic and mass number of the material traversed;  $r_e$  is the classical electron radius;  $\alpha$  is the differential cross-section and  $X_0$  is the radiation length [2]. This is a derivation from the Bethe-Bloch formula with  $\beta$  set to 1 as  $v \approx c$

In the regime of ultra-relativistic velocities, ionization losses can be neglected and the energy loss can be given by the radiation length

$$\frac{dE}{dx} = -\frac{E}{X_0} \quad (2)$$

Hence, the sum of all path lengths in an electron shower is a measure of the energy deposited by the traversing particle.

Hadronic showers occur when high energy hadrons (above 5MeV) such as  $\pi^-$  or an atomic nucleon traverse a dense material. In these events, elastic interactions as well as inelastic interactions take place between the particle and the nucleons of the material [2]. While the details are more complex than that of the electromagnetic shower, the hadronic shower is similar in that it involves incident particles interacting and producing a multitude of less energetic hadrons. Hadron showers are characterized by their interaction length  $I_A$ . As with the EM shower, the shower extends into the medium until all the energy is absorbed albeit at a much greater depth. [2]

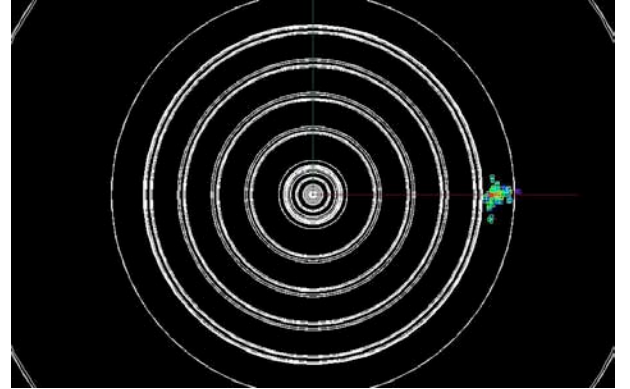


FIG. 1. Figure showing an example of an EM shower in particle detector. The observed track is that of a 1 GeV electron

While their designs may vary, high energy calorimeters are usually composed of an electromagnetic section and a hadronic section. The electromagnetic calorimeter (ECAL) is designed to measure the energy deposited by particles that primarily produce electromagnetic showers while the hadronic calorimeter (HCAL) primarily function to measure the energy deposited by hadronic showers. The energy measured by the calorimeters comes

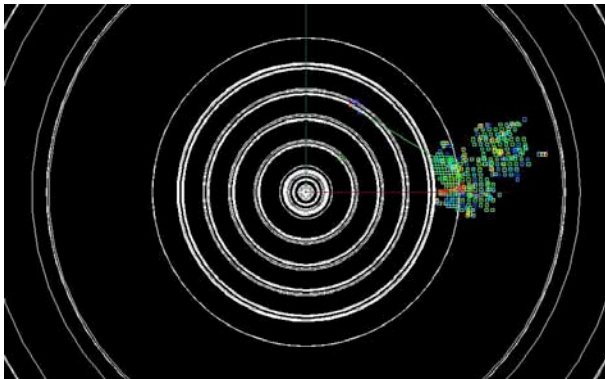


FIG. 2. Figure showing an example of an hadronic shower. The observed track is that of a  $1 \text{ GeV } \pi^-$

from the *scintillation photons* released from the showers. Scintillation photons are emitted after the atoms in the material are excited by the energy absorbed from the showers. For electrons, virtually all the energy is released as scintillation photons. This fact makes measuring the energy deposited by passing electrons relatively simple. However, hadronic showers involve interactions that don't always produce scintillation photons in the end. The energy consumed by these interactions is not measured by the calorimeter and this unaccounted leads to less a precise energy measurement. Hence, measuring the scintillation light emitted from a hadron shower will very likely only represent a fraction of the energy deposited. For these reasons, current EM calorimeters are capable of much better energy resolution than current hadron calorimeters.

For hadron colliders such as the Tevatron and the LHC, there are many external uncertainties that limit the energy resolution of calorimeters making the relatively poor energy resolution of hadronic calorimeters somewhat inconsequential. However, future lepton colliders such as the International Linear Collider (ILC) will feature much more precise collisions and require much more precise energy measurements than current hadronic calorimeters can afford [3]. The low ILC backgrounds will open up new possibilities of associating tracks and calorimeter clusters. Excellent energy resolution is essential for the identification of many decay channels at the ILC. Having such resolutions enhances the impact of precision measurements and lowers the luminosity required for many measurements [3]. To meet this challenge, the concept of the dual readout calorimeter is proposed. In particular, this research effort proposes a totally active dual read out crystal calorimeter otherwise known as the CCAL02 detector, which will be capable of functioning as a high precision EM and Hardon calorimeter [4].

## THE CONCEPT OF THE DUAL READOUT CALORIMETER

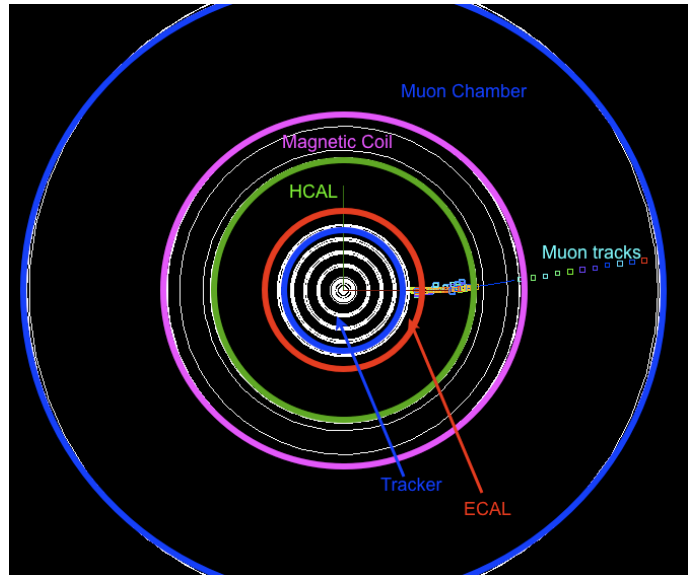


FIG. 3. Diagram representing a cross-sectional view of the proposed CCAL02 detector. The inner most rings represent the tracker. The subsequent layers are the EM calorimeter and its larger counterpart the HCAL calorimeter. Outside the HCAL calorimeter are magnetic coils and the muon chamber. The track seen in this diagram is that of a  $5 \text{ GeV}$  muon.

A diagram of the proposed detector is shown in figure 3. The main interest of this analysis project will be the ECAL and HCAL layers. Two key features of the proposed dual readout calorimeter is that it is totally active and finely segmented. It is totally active in the sense that the material used to generate the particle showers is the same as the material used to detect and measure the deposited energy. It is not considered totally absorbing since it might be infeasible to construct a large enough or dense enough calorimeter to contain all showers. The calorimeter will feature longitudinal segmentation, which will be helpful in correcting for leakage [4]. The design also features further lateral segmentation, creating many smaller calorimeter cells. Each cell is to be coated with a photo-reflective material and equipped with its own photo-detector, making each cell essentially an independent calorimeter. This design feature opens the door for many additional capabilities namely the capacity to apply particle flow algorithms (PFAs).

As previously stated, the light measured by the calorimeters is in the form of scintillation light. For electrons, this is a precise measure of the energy deposited by their EM showers. Another source of light is Cherenkov light which comes about when a charged particle traverses a medium faster than the speed of light in that particular medium. The term dual readout refers to the

calorimeter's capability of measuring both the Scintillation and Cherenkov light. Because of their relatively low masses, electrons and positrons from the EM showers tend to be the particles radiating Cherenkov light. Hence, Cherenkov light presents itself as another measure of the electromagnetic shower of any shower. More importantly, Cherenkov light is also a more precise measure of the energy deposited. By measuring the Cherenkov and scintillation responses of electrons of known energies, the relationship between the both signals and the energy deposited by the EM showers can be established. When the responses are measured for pions of known energies, they will only represent the electromagnetic portion of the shower. However, by using the relationships determined from the electron calibration and by comparing the ratio of the measured scintillation energy and the incident energy of the pion with the ratio of scintillation light and Cherenkov light for different pion energies, a correction function can be obtained. This correction function is referred to as the dual readout correction function and when applied to the energy response from a hadron shower, the energy lost to nuclear interactions can be determined to relatively good precision.

## SIMULATING THE DUAL READOUT CALORIMETER

### Detector Configuration

For our simulation study the detector configurations used are outlined in the table I below:

TABLE I. Table showing detector configuration.

| <i>Name</i>  | <i>layers</i> | <i>Length (cm)</i> | <i>Depth (cm)</i> | <i>Seg. (cm)</i> |
|--------------|---------------|--------------------|-------------------|------------------|
| Ecal Barrel  | 8             | 3                  | 24                | 3 x 3            |
| Hcal Barrel  | 17            | 6                  | 102               | 5 x 5            |
| Total Barrel | 25            |                    | 126               |                  |
| Ecal Endcap  | 8             | 3                  | 24                | 3 x 3            |
| Hcal Endcap  | 17            | 6                  | 102               | 5 x 5            |
| Total Endcap | 25            |                    | 126               |                  |

To construct the dual readout calorimeter, a radiator capable of producing both scintillation and cerenkov is required. Among many other considerations, such a material has to be consistently functional in a high energy collider environment. Several materials show potential of meeting all these requirements. Of particular interest is Bismuth Germanate (*BGO*) and Lead Tungstate (*PbWO<sub>4</sub>*) [4]. For this design the ECAL and the HCAL are made of the same crystals. The material properties of some crystals considered are shown in Table II.

The calorimeter was simulated using an extended version of the American Linear Collider Physics Group (AL-

TABLE II. Table showing material properties of calorimeter crystals.

| <i>Material</i>         | <i>Density (g/cm<sup>3</sup>)</i> | <i>Rad.Length (cm)</i> | <i>IALength (cm)</i> |
|-------------------------|-----------------------------------|------------------------|----------------------|
| <i>BGO</i>              | 7.13                              | 1.12                   | 21.88                |
| <i>PBWO<sub>4</sub></i> | 8.3                               | 0.9                    | 18                   |

CPG) software suite [5]. The ALCPG suite consists of the Simulator for the Linear Collider (SLIC) package, lcsim.org package and the Java Analysis Studio (JAS3) [6] analysis framework. SLIC is a simulation package that uses the Geant4 Monte Carlo toolkit to simulate the passage of particles through different media. The physical processes used by SLIC are defined by different physics lists. The lcsim.org [7] package is used for reconstruction and analysis and is built entirely on the Java platform. JAS3 is a open source, general purpose data analysis framework used for data analysis, event display and features an event browser.

### Physics Lists

A major challenge in simulating any calorimeter is the choice of an appropriate physics list. Physics lists define the physical processes that occur in the simulations. The goal of every physics list is to construct a physical environment that exactly matches the environment seen in an actual experiment. Though many physics lists come close to recreating a fully realistic physical environment, none have been able to achieve the status of being completely realistic. Many physics lists are available on the market and each has its strengths and weaknesses. The main physics list used for this project was the FTFP\_BERT.

For the simulations used in this project, the particles were fired radially from beginning of the EM calorimeter. This was done primarily to avoid dealing with the complications of interaction events in the tracker. The first set of simulations were done for  $\pi^- \pi^-$  and electrons at set energies (1, 2, 5, 10, 20, 50 and 100 GeV) with 10,000 events for each. These simulations were done with *BGO* crystals defined in table II. The simulation files were saved as .slcio files, which would be later used for analysis.

## ANALYSIS

The analysis was done using the org.lcsim package in Netbeans and JAS3. The following sections will outline the main analysis procedure of obtaining the dual read out correction.

### Dual Readout Correction Process

The dual readout correction process consists of the following steps:

1. Calibrating the calorimeter response using electrons.
2. Obtaining the dual readout correction function for hadrons ( $\pi^-$ ).
3. Applying the correction to the scaled energy response.
4. Obtaining the energy resolution of the corrected energy response.

#### Electron Calibration

The calibration step involves finding scale factors that normalize the cerenkov and scintillation signals. Electrons of various energies are simulated and their digitized energy responses are plotted as shown in figure 4. Details about the digitization process will be explored in the following section. To get the scale factors, plots of the cerenkov and scintillation responses are made against incident energy. The relationship is then parametrized by first order polynomials whose coefficients are taken as the scale factors. Figure 5 shows a plot of the corrected cerenkov  $C$  energy against the corrected scintillation energy  $S$  of a 1 GeV electron.

As expected from the two well defined responses seen in figure 4, this figure produces a well defined spot. The scaled factors are then used to scale the responses of  $\pi^-$ . A plot (figure 6) of fraction ( $S/E$ ) versus ratio ( $C/S$ ) is made for the  $\pi^-$  of multiple energies. The first plot in the top left of figure 6 is that of a 1 GeV electron. The bottom left plot is for all energies combined. The significant spread in the  $\pi^-$  plots are representative of the hadronic showers. Unlike electrons,  $\pi^-$  interact with nuclei in the medium. The lateral spread observed in the  $\pi^-$  plots are a result of the energy "lost" to these nuclear interactions.

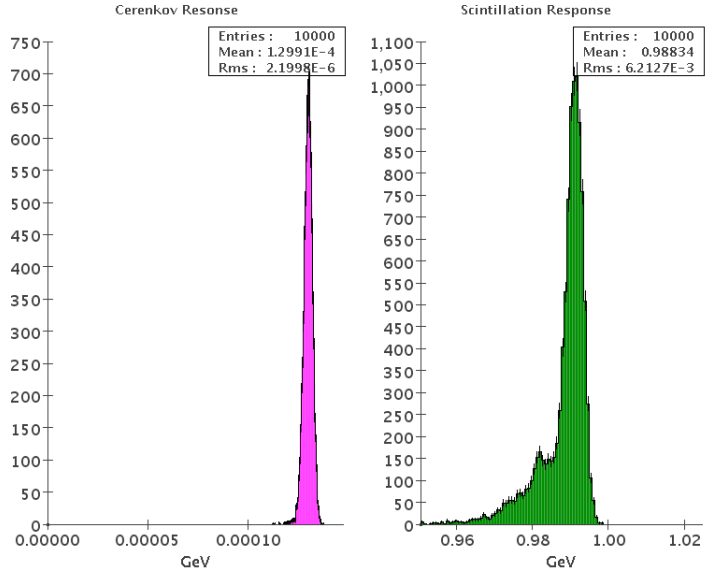


FIG. 4. Figure showing the scintillation and cerenkov response for 1 GeV electron done for 10000 events. The figure on the left shows the Cerenkov response and the figure on the right shows the Scintillation response. The mean scintillation response is very close to the incident energy as one would expect. One should note the differences in the x-scales of the two plots.

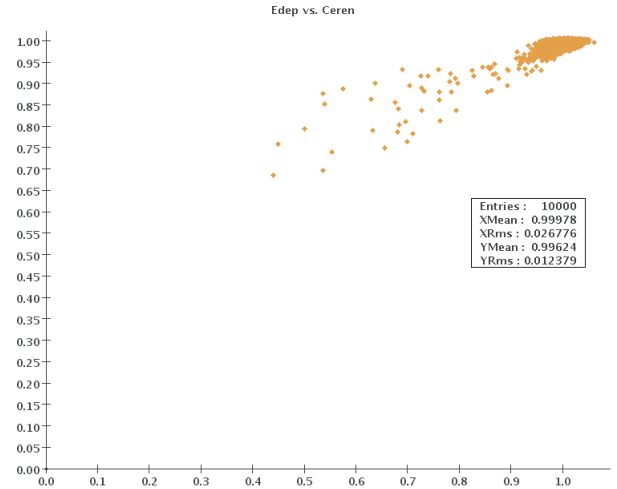


FIG. 5. Figure showing the plot of the scaled scintillation response  $S$  against the scaled cerenkov response  $C$  for a 1 GeV electron.

#### Obtaining the dual readout correction function

Obtaining the correction function involves several steps. First, the fraction vs ratio plot is divided into slices along the x-axis. For our analysis, 25 bins were used and ratio greater than 1 was automatically placed in the final bin. The y-axis projection of each slice is then converted into a histogram. The

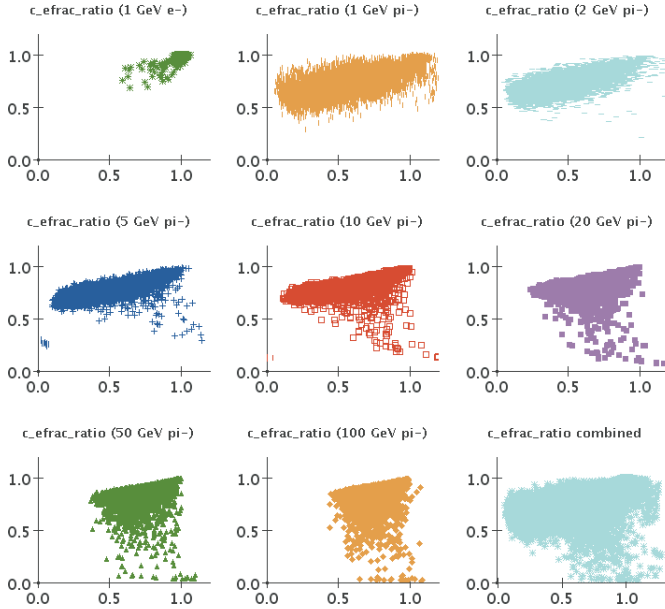


FIG. 6. Figure showing the plots of fraction  $S/E$  against ratio  $C/S$  for various energies. The top left plot is that for a 1 GeV electron. Going from left to right the plots shown are for 1, 2, 5, 10, 20, 50 and 100 GeV  $\pi^-$ . The bottom right plot is that for all the energies combined.

mean of the distribution within each slice is obtained and is plotted against its corresponding ratio. The points are fit with a polynomial whose equation is taken as the correction function. Figure 7 shows the correction functions obtained for  $\pi^-$  of different energies.

#### Getting the corrected energy response

A correction function is obtained for each incident energy. The correction function used to correct the energy responses is the one obtained from the composition of all energies. This function takes the form of

$$P(x) = 0.5763 + 0.6017x_1 - 0.5306x_2 + 0.4808x_3 - 0.10252x_4. \quad (3)$$

To get the corrected scintillation response  $S_c$ , we use

$$S_c = \frac{S}{P\left(\frac{C}{S}\right)}. \quad (4)$$

Here,  $\frac{C}{S}$  is taken as the the argument of equation 3.

Figure 8 shows the plots of the  $\pi^-$  scintillation energy for each incident energy before and after the correction. For each response the plot is approximately Gaussian and their mean is close to the incident energy. As expected the uncorrected responses have means less than the incident energy which is reflective of the energy lost to nuclear reactions. After the correction function

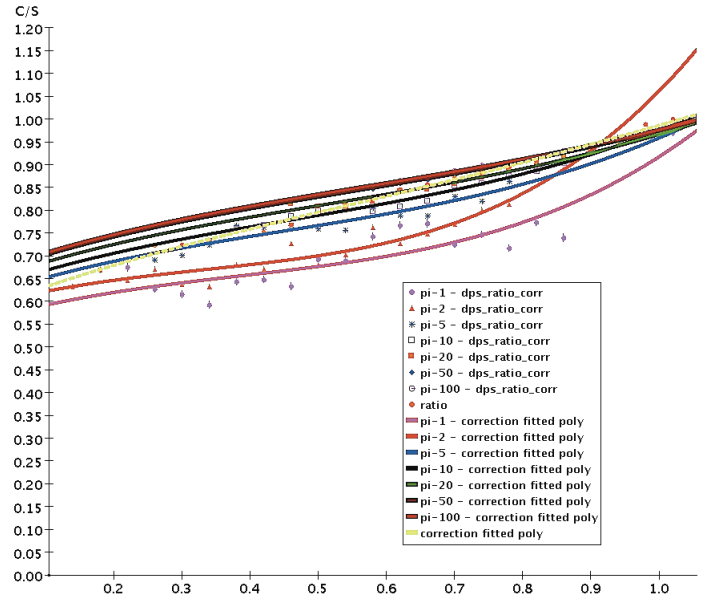


FIG. 7. Figure displaying the fraction mean against each ratio for 1, 2, 5, 10, 20, 50 and 100 GeV  $\pi^-$ . The relationships are parameterized by 4<sup>th</sup> order polynomials whose equations are taken as the correction functions. The dashed line is the correction function obtain from the combination of all  $\pi^-$  energies.

is applied, the energy responses shift closer to the mean of the incident energy as expected.

A closer inspection of figure 8 reveals another interesting finding. For higher energies, the responses have a pronounced leading tail. This would suggest that there are still many events that produce energies much lower than the incident energy even after the correction function has been applied. This lost energy can be attributed to leakage, which refers to the instances where the incident  $\pi^-$  is not to totally absorbed and escapes the calorimeter with some amount of its energy intact. This is no doubt an issue that needs to be addressed as this energy loss inevitably decreases the calorimeters energy resolution.

#### Taking a closer look at the digitization

##### Raw hit corrections

The next step in the project was to examine the effect of the digitization cuts. The digitization of the energy values involved applying energy and time threshold cuts to the raw energy values read out from each cell. Initially, the energy threshold cut was set at 1/50 of the average energy deposited by a minimum ionizing particle (mip) while the time cut was set at 100ns. In



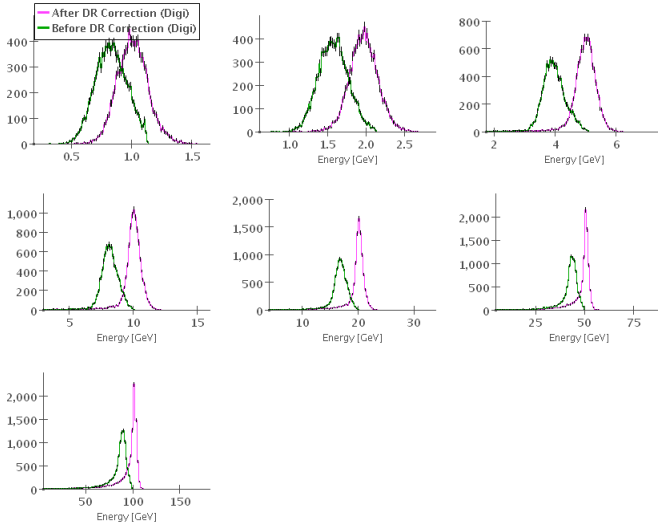


FIG. 8. Figure illustrating the plots of the corrected (pink line) and uncorrected (green line) scintillation energy response of 1, 2, 5, 10, 20, 50 and 100 GeV  $\pi^-$ .

the EM calorimeter, the mip value was determined to be roughly 30MeV while in the hadronic calorimeter it was approximately 60MeV. The difference in energy values is a result in the difference in cell sizes in both calorimeter sections. Figure 9 shows a comparison of the scintillation response with and without digitization cuts. As one would expect, the raw energy response has a greater mean than the digitized response. For lower energies, below 10 GeV, this difference is much more emphasized due to the fact that the digitization cuts are removing a larger percentage of the incident energy.

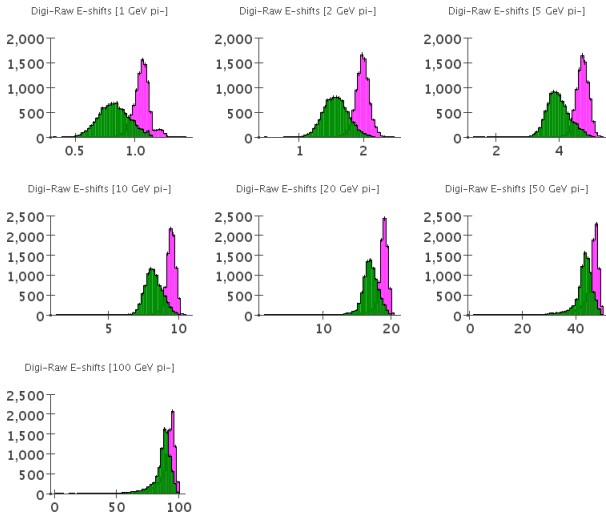


FIG. 9. Figure illustrating the raw (pink) and digitized (green) scintillation response for 1, 2, 5, 10, 20, 50 and 100 GeV  $\pi^-$ .

The dual readout correction process was repeated using the raw energy values and a new correction function was obtained. The digitized and raw correction functions are shown in figure 10. The functions were fitted with a 4<sup>th</sup> order polynomial but as one could imagine these relationships could easily be parameterized by a first order polynomial which is shown in subsequent figure. For consistency, the 4<sup>th</sup> order approximation was used to do the correction.

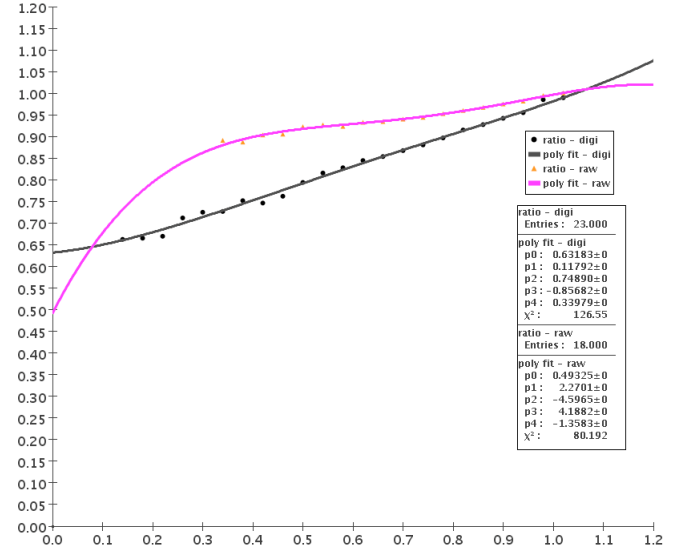


FIG. 10. Figure showing the raw (pink) and digitized (black) correction function for combined  $\pi^-$  energies. The relationships were parameterized by 4<sup>th</sup> order polynomials.

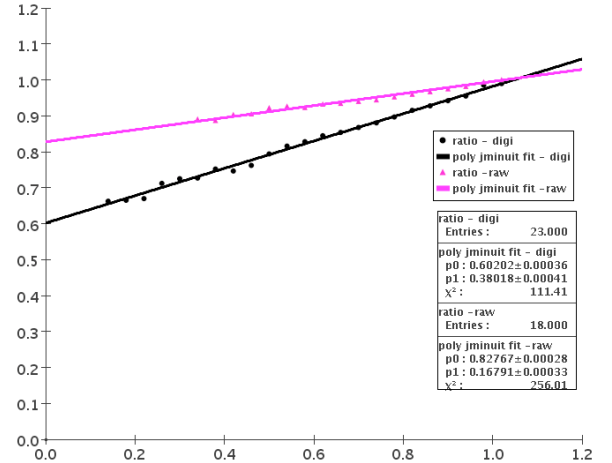


FIG. 11. The above figure shows the raw (pink) and digitized (black) correction function for combined  $\pi^-$  energies. The relationships were parameterized by 1<sup>st</sup> order polynomials

Figure 12 shows a comparison of the corrected raw and

digitized energy responses. As expected the correction function for the raw distribution is greater than that of the digitized distribution. This is because the raw energy responses have a greater scintillation response  $S$  and as a result greater fraction  $\frac{S}{E}$  values. One would expect that if each response was treated with its own correction function, the final corrected energies would be approximately the same. It turns that this was only true for energies greater than 10GeV. Below 10 GeV there was still a marked and unaccounted difference between the two corrected energy responses. To test if this was an artefact of the applied correction function, the first order polynomial correction functions for the raw and digitized hits were applied to the scintillation responses. This is shown in figure 13 and as one can observe the discrepancies only got worse.

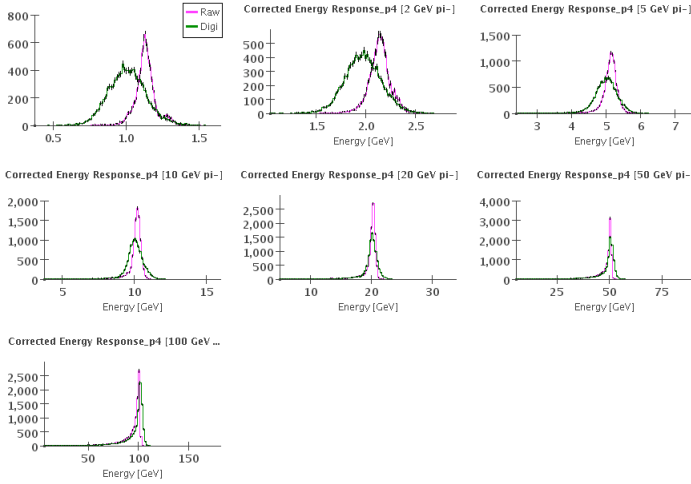


FIG. 12. Figure showing the raw (pink) and digitized (pink) corrected scintillation response for 1, 2, 5, 10, 20, 50 and 100 GeV  $\pi^-$ . The correction function used was a 4<sup>th</sup> order polynomial.

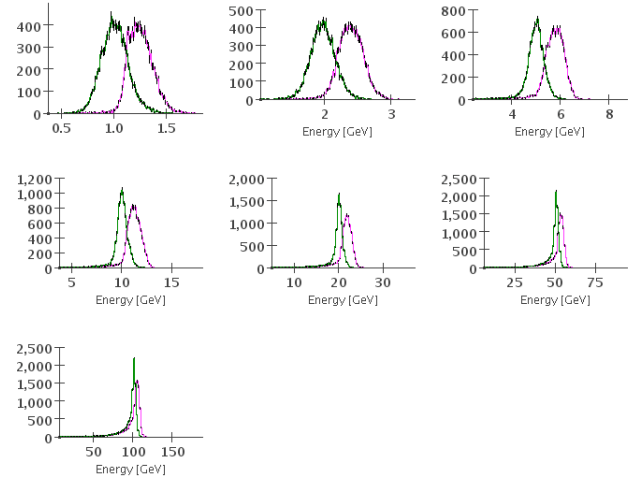


FIG. 13. Figure showing the raw (pink) and digitized (pink) corrected scintillation response for 1, 2, 5, 10, 20, 50 and 100 GeV  $\pi^-$ . The correction function used was a 1<sup>st</sup> order polynomial.

### Analysis of minimum ionizing particle: Muon runs

Next, we sought to observe the effect of the digitization cuts on the minimum ionizing particles. A 5GeV muon was simulated for a 1000 events and passed on for analysis. Figure 14 shows an image of one the events. For this analysis we were interested in seeing the effect of the digitization on the energy distribution per cell. Figure 15 shows the pulse height seen per cell with and without the digitization cuts. Here a very large portion of pulse heights are observed near zero. With the threshold cuts, this spike near zero is still very predominant. Figure 16 shows pulse height as a function of time without the digitization and figure 17 shows the same plot with the digitization.

The energy threshold values were varied and the resulting energy distribution was observed. The time cut was held constant at 100ns and the energy thresholds were varied from  $\frac{1}{50}$ ,  $\frac{1}{25}$ ,  $\frac{1}{10}$ ,  $\frac{1}{2}$  of a mip to 1 mip. Figure 18 shows plots of the energy distribution per cell for in the EM calorimeter (ECAL) and figure 19 shows the distribution for the Hadronic Calorimeter (HCAL). Figure 20 shows the fraction of energy lost in the ECAL and HCAL due to each threshold cut. Here we observe that for threshold cuts below  $\frac{1}{10}$  of a mip the energy lost is approximately below 10% but for 1 mip threshold cut losses of 60% is seen in the ECAL and 40% in the HCAL.

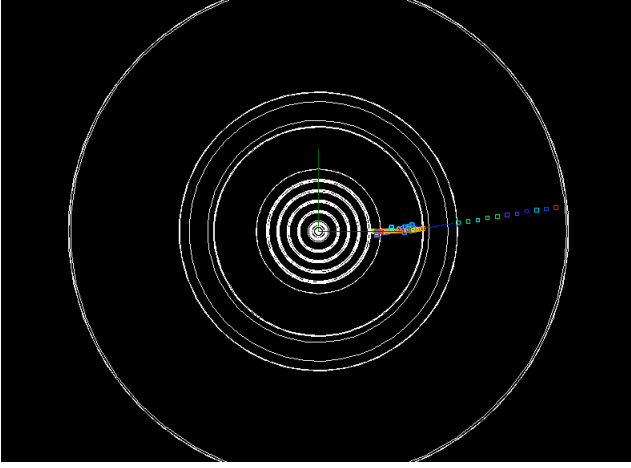


FIG. 14. Figure showing a simulated event of a 5 GeV muon going through the detector. The track begins at the inner radius of the the EM barrel, passes the through the Hadron barrel, then through the magnetic coils and finally through the muon chamber.

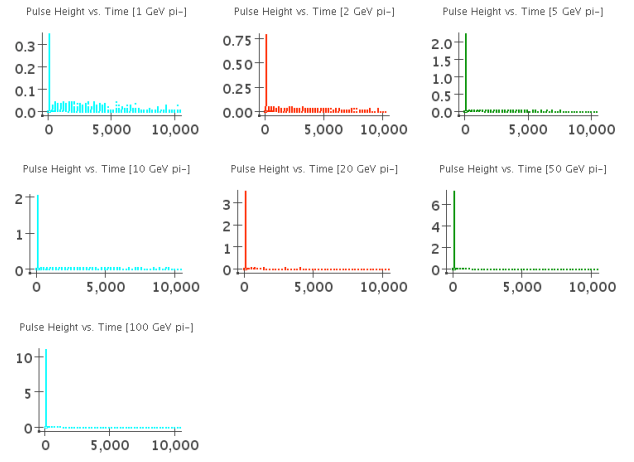


FIG. 16. Figure showing the pulse height as a function of time without the threshold cuts.

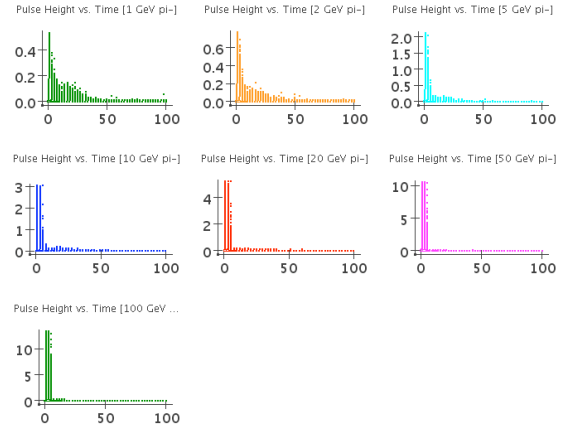


FIG. 17. Figure showing the pulse height as a function of time with the digitization threshold .

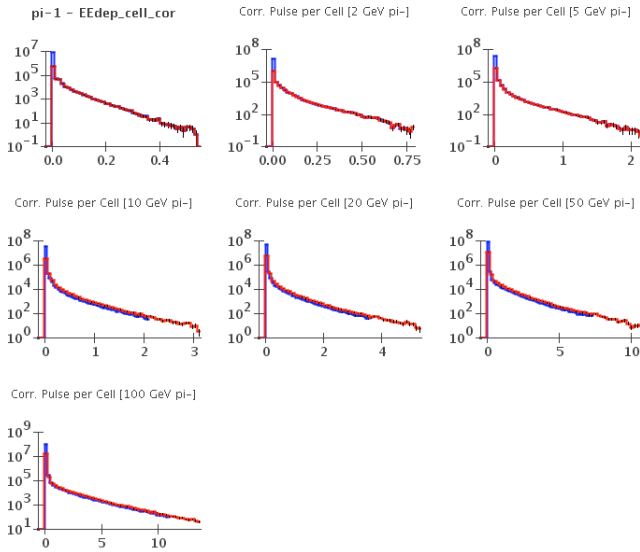


FIG. 15. Figure showing pulse height seen per cell with and without the digitization cuts.

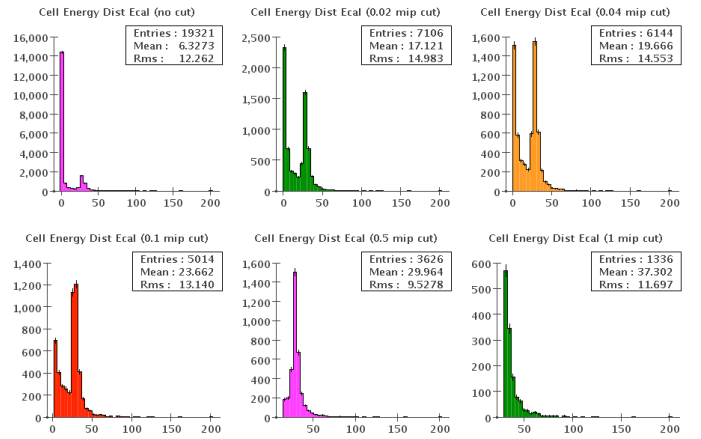


FIG. 18. Figure showing pulse height seen per cell for different energy threshold cuts in the ECAL. Here the energy thresholds were varied from  $\frac{1}{50}$ ,  $\frac{1}{25}$ ,  $\frac{1}{10}$ ,  $\frac{1}{2}$  of a mip to 1 mip

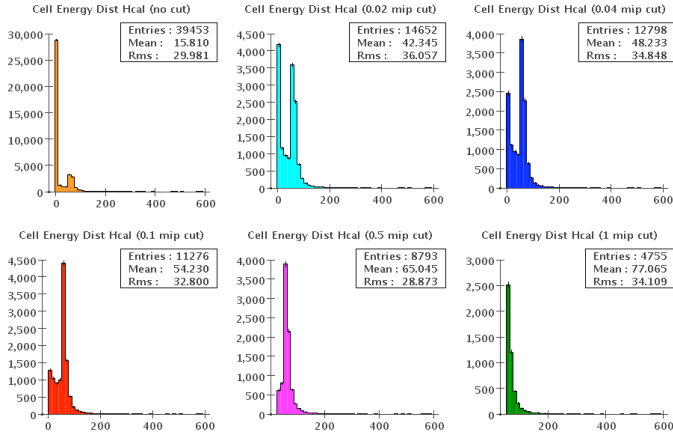


FIG. 19. Figure showing shows pulse height seen per cell for different energy threshold cuts in the HCAL. Here the energy thresholds were varied from  $\frac{1}{50}$ ,  $\frac{1}{25}$ ,  $\frac{1}{10}$ ,  $\frac{1}{2}$  of a mip to 1 mip

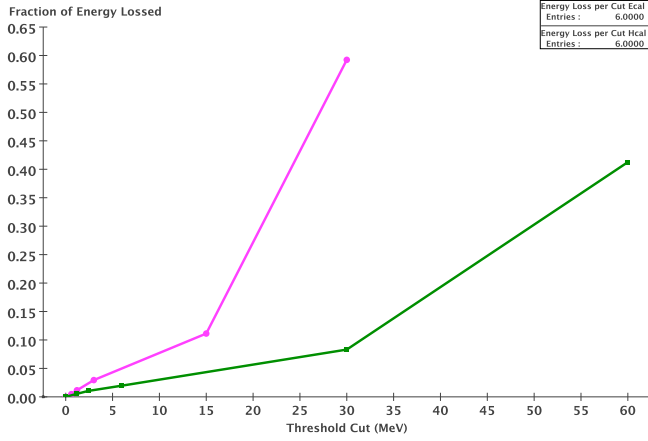


FIG. 20. Figure showing the fraction of energy lost per threshold cut. Here the energy thresholds were varied from  $\frac{1}{50}$ ,  $\frac{1}{25}$ ,  $\frac{1}{10}$ ,  $\frac{1}{2}$  of a mip to 1 mip

### Cell analysis

Next we sought to find the source of the very large spike in the energy response histogram near zero for the low energy threshold cuts. We postulated that these low energy responses were from the cells that were just clipped by the passing muons. That is, the muons only managed to travel through a very small portion of these cells and as a result only deposit a very small portion of energy. To remove the influence of the lateral segmentation, the energy response from each layer was investigated. Figure 21 shows the energy distribution per layer for the  $\frac{1}{50}$  of a mip threshold cut. Here no spike near zero is observed, confirming the aforementioned hypothesis.

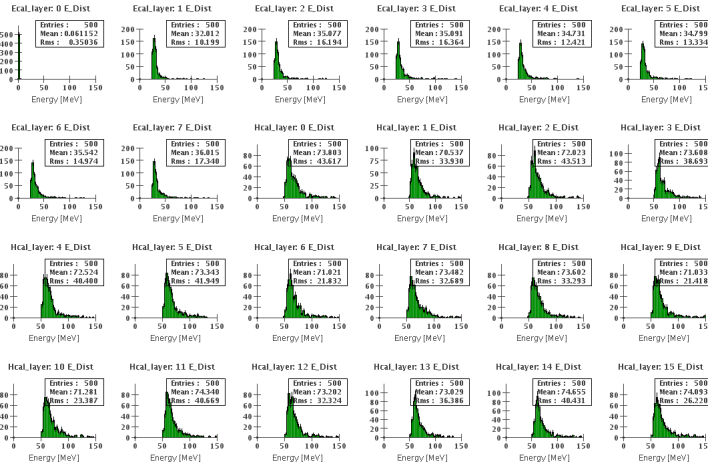


FIG. 21. Figure showing plots of the energy distribution per layer for the  $\frac{1}{50}$  of a mip threshold cut. The first 8 layers are from the ECAL and the remaining 17 are from the HCAL (the 25<sup>th</sup> layer is not shown).

### The effect of energy threshold cuts on the energy resolution 20 GeV $\pi^-$

For our final analysis, the energy threshold values were varied for the  $\pi^-$  with the intention of observing the effect on the energy resolution. The 20GeV  $\pi^-$  simulation file was selected and energy threshold cuts of  $\frac{1}{50}$ ,  $\frac{1}{25}$ ,  $\frac{1}{10}$ ,  $\frac{1}{2}$  of a mip and 1 mip were applied. For each threshold cut the dual readout correction process was applied and each energy response was corrected with its own correction function. Figure 22 shows the corrected energy response for each threshold cut overlaid with a Gaussian fit. Figure 23 shows the sigma of the energy response for each threshold cut. With no energy threshold cuts, the sigma value of the fit was approximately 0.535. This corresponds to energy resolution of  $\frac{E(\sigma)}{E} = \frac{0.11}{\sqrt{E}}$ . With a

1 m.i.p. cut the energy resolution was  $\frac{E(\sigma)}{E} = \frac{0.5}{\sqrt{E}}$ .

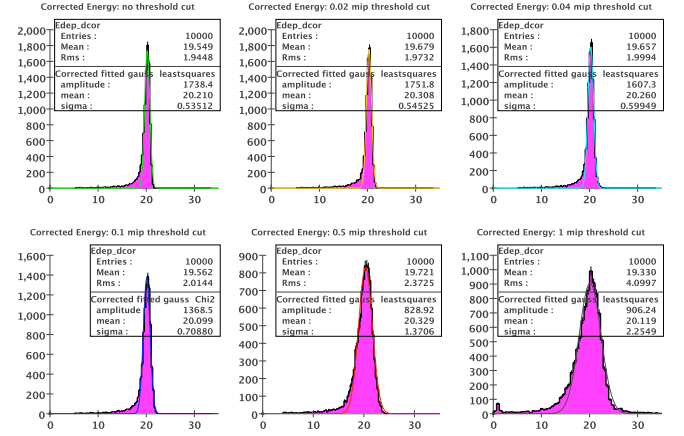


FIG. 22. Figure showing plots of the corrected energy response for each threshold cut.

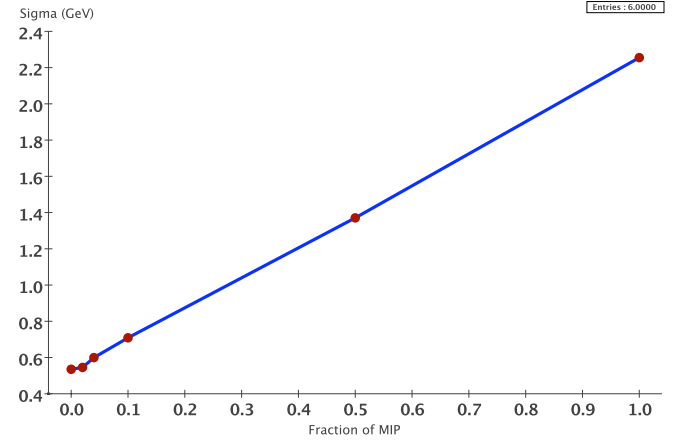


FIG. 23. Figure showing the sigma of the corrected energy response for each threshold cut.

## CONCLUSION

### Summary of results and analysis

Our analysis of the ccal02 totally absorbing calorimeter revealed key insights to its physical nature and broadened our understanding of the limitations of the detector. Moreover, this analysis has improved our understanding of the simulation and analysis process itself. By comparing the raw energy response with the digitized response, we observed that the energy threshold cut of  $\frac{1}{50}$  of a mip had a very pronounced effect on lower (below 10 GeV) energy  $\pi^-$ . When the dual readout correction process was applied to both the digitized and raw response, the final corrected response did not align as expected for all energies. For  $\pi^-$  energies below 5 GeV, the means corrected raw energy response was markedly higher than the digitized energy responses. The cause of this is still unclear but one possible source might be the simulation process itself at these low energies.

Upon analyzing the simulation of a 5GeV muon, we learned the effect of energy threshold cuts on the energy distribution throughout the calorimeter cells. We observed that a significant number of cells registered minute energy responses for each event. It was revealed that these small energy response are a result of when the m.i.p. only traverses a small portion of the cell, managing only to deposit a small amount of energy. This effect proved to be very significant once the energy threshold cuts were applied. For threshold cuts up to about  $\frac{1}{10}$  of a m.i.p. the energy lost was at or below 15% in both barrels. At a threshold cut of 1 m.i.p., the energy loss was about 40% in the HCAL and 60% in the ECAL.

Upon varying the digitization threshold cuts were varied for 20GeV  $\pi^-$ , we found that the resolution varied from  $\frac{E(\sigma)}{E} = \frac{0.11}{\sqrt{E}}$  for no threshold cuts to  $\frac{E(\sigma)}{E} = \frac{0.5}{\sqrt{E}}$  for a 1 m.i.p threshold cut.

### Future work

At the conclusion of this analysis, many insights were made but an even greater number of questions remain

unanswered. One challenge in determining the correction function was dealing with the energy leakage. In the case of the  $\pi^-$ , the presence of leakage at higher energies complicated our analysis of the dual readout correction process as it presented a new form of energy loss. For future work, it would be beneficial to analyze simulations where there is no leakage so as to decouple the two energy losses. Leakage can be removed either by simulating a larger detector or by using crystals with greater density.

When the dual readout process was applied to both the raw and digitized energy responses, the final corrected energy responses were not aligned at low energies. A lack of a sufficient explanation of this occurrence warrants further investigation into the matter.

More analysis needs to be done to account for changes in photon statistics. In particular, the losses as photons traverse the crystals and enter the photodetectors need to be examined as this will also contribute to the final energy resolution.

---

\* eaw2161@columbia.edu

- [1] C. A. et al., Physics Letters **592**, 1 (2008).
- [2] K. Kleinknecht, *Detectors for Particle Radiation* (Cambridge University Press, 1998).
- [3] G. Aarons, T. Abe, J. Abernathy, and M. Ablikim, "International linear collider reference design report: Physics at the ilc," (2007), iLC design report.
- [4] A. Para, H. Wenzel, and E. R. a, "Simulation of a totally active dual read out calorimeter for future lepton colliders," Preprint submitted to Nuclear Physics B.
- [5] <http://physics.uoregon.edu/~lc/alcpag/>.
- [6] <http://jas.freehep.org/jas3/>.
- [7] <http://www.lcsim.org/software/lcsim>.